Measurements of Bulk Fluid Motion in Direct-Drive Implosions

Introduction

In inertial confinement fusion (ICF) experiments performed on OMEGA, a spherical shell of deuterium–tritium (DT) ice or CH plastic is filled with DT gas. A laser illuminates the shell, applying an ablative pressure that accelerates the shell radially inward. As the shell converges, it compresses the DT gas, converting its kinetic energy into thermal energy of the gas. This spherical compression produces a hot spot at temperatures and densities that allow fusion reactions to occur.

To achieve maximum conversion of a shell's kinetic energy to hot-spot thermal energy, a spherically symmetric implosion is desired. In reality, implosions suffer from both low-mode[1] and high-mode[2] asymmetries, which degrade implosion performance. Understanding and measuring the degradation in performance caused by real world asymmetries are vital to optimize direct-drive implosions and constrain theoretical models.

Bulk collective motion of the hot spot is characteristic of implosions with low-mode asymmetries.[3,4] Measurements of bulk collective motion in ICF experiments would confirm the existence of low-mode asymmetries and give indications of the perturbation strength. This work describes a method to measure bulk collective motion of the hot spot in ICF experiments by measuring the primary DT fusion neutron energy spectrum.

The neutron energy spectrum produced by a stationary fusing fluid element was studied non-relativistically by Brysk[5] and semi-relativistically by Ballabio.[6] The neutron energy spectrum produced by a moving fusing fluid element was studied fully relativistically by Appelbe[7,8] and Munro.[9,10] These results showed that the shape of the neutron energy spectrum is approximately Gaussian with moments that depend not only on the plasma ion temperature but also on the fluid element velocity. In particular, if the fluid element is moving with a bulk collective motion, the first moment of the neutron energy spectrum is shifted depending on the magnitude of the projection of the fluid velocity along the measurement axis.

The relationship between the fluid element velocity and the corresponding neutron energy shift has been derived non-relativistically by Murphy[11] and relativistically by Zylstra.[12] Assuming all bulk collective motion is along the line of sight (LOS) of the measurement, the relativistic relationship can be written as

$$v_f = \frac{v - v_0}{1 - v v_0}, \tag{1}$$

where v_f is the fluid element bulk flow velocity in the lab frame, v is the measured neutron velocity in the lab frame, and v_0 is the neutron velocity in the fluid element frame. The neutron velocity is related to the mass normalized neutron energy $\chi = E/m_{\mathrm{n}}$ by

$$v = \frac{\sqrt{\chi^2 + 2\chi}}{\chi + 1}. \tag{2}$$

By using Eqs. (1) and (2), shifts in the neutron energy spectrum can be interpreted as bulk collective motion of the fusing fluid element.

In ICF experiments there is not just a single fusing fluid element; instead there is a collection of fusing fluid elements within the hot spot that are distributed in space and time. Since measurements of the neutron energy spectrum are both spatially and temporally integrated, we interpret shifts in the first moment of the neutron energy spectrum as the neutron-averaged hot-spot bulk collective fluid velocity.

Simulations of cryogenic OMEGA implosions with low-mode asymmetries caused by real world effects such as laser illumination nonuniformity, target offset, and ice roughness showed neutron-averaged hot-spot bulk collective motion as large as 100 km/s along particular measurement axes.[4] Previous measurements of shifts in the first moment of the neutron

energy spectrum by nuclear recoil spectroscopy inferred bulk collective motion as large as 210±30 km/s in polar-direct-drive (PDD) experiments at the National Ignition Facility (NIF),[13] while measurements by a similar method in direct-drive experiments on OMEGA lacked the energy resolution required to measure fluid velocities relevant on OMEGA.[12]

In this article we present measurements of shifts in the first moment of the neutron energy spectrum using the neutron time-of-flight (nTOF) technique.[14] The following sections (1) describe a new nTOF detector fielded on OMEGA that measures bulk collective motion of the hot spot; (2) describe the detector calibration including measurements of the detector instrument response function (IRF) and the absolute timing calibration; (3) report measurements of bulk collective motion in cryogenic implosions; and (4) present conclusions and discuss an extension of this method to four lines of sight.

Detector Design

The neutron energy spectrum produced in OMEGA implosions is measured using a series of nTOF spectrometers.[15] Recent increases in neutron yields greater than 10^{14} on OMEGA have provided high neutron statistics for the nTOF detectors.[16]

A new nTOF detector has been built to take advantage of the increased neutron yield. By decreasing the scintillator volume, the new detector provides a fast IRF of 1.7-ns full width at half maximum (FWHM) while maintaining a large signal-to-noise ratio for neutron yields between 10^{10} to 10^{14}. A fast instrument response minimizes the distortion of the incoming primary DT neutron signal, which has a FWHM between 2 to 4 ns, by the detector IRF and therefore makes it possible to accurately measure the primary DT neutron energy spectrum.

The new detector consists of a 50-mm × 50-mm × 5-mm quenched plastic scintillator [EJ-232Q-1% (BC-422Q)] (Ref. 17), attached to a 15-cm acrylic light guide, which is coupled to a Photek 140 photomultiplier tube (PMT).[18] The PMT is operated at a constant bias of –4.7 kV to ensure a stable PMT response and sufficient gain. The PMT signal is transported to a four-channel 10-GSamples/s Tektronix oscilloscope by a 5-m LMR-400 coaxial cable. To maximize light collection efficiency, the entire scintillator and light-guide connection is covered in a light-tight wrapping. The detector design is shown in Fig. 154.68.

The detector is located in a well collimated LOS 13.0 m from target chamber center (TCC) in the southern hemisphere of the OMEGA target chamber along the P7 port. This is the only shielded LOS on OMEGA and allows for all relevant electronics, including the PMT, to be out of the LOS of the primary neutron beam while also minimizing the signal from scattered neutrons. The combination of these two features results in an extremely high-quality signal.

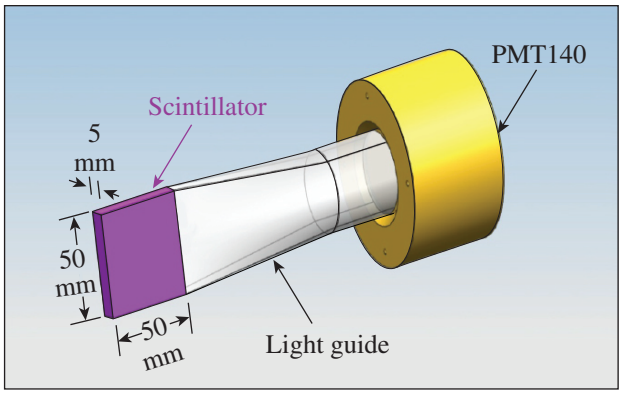

Figure 154.68
The detector design consists of a small quenched plastic scintillator (purple) connected to a light guide, which is connected to a photomultiplier tube (PMT140) (yellow).

Detector Calibration

1. Instrument Response Function

The IRF can be constructed by considering the detector's neutron and photon responses. The neutron response measures the neutron transit time through the detector, while the photon response measures the recorded electronic signal as a function of time for an impulse photon signal. The actual IRF is a convolution of these two components.[19]

Due to the thin scintillator design, the transit time of a 14-MeV neutron through the scintillator is ~100 ps. This results in the average number of neutron interactions within the scintillator being 1 and the neutron response being well approximated by a delta function in time. For this reason the IRF for this detector is simply the photon response.

The detector photon response, and therefore the detector IRF, has been measured *in situ* by recording the detector response to x-ray impulse signals created by illuminating a Au sphere or Au foil with a 20- or 100-ps-long Gaussian laser pulse. The x-ray signal produced in these experiments had a temporal width between 70 and 100 ps as measured by the neutron temporal diagnostic (NTD).[20] The x-ray signals produced in these experiments, therefore, approximate a delta function in time incident on our detector so the recorded signal is a direct measurement of the IRF.

The detector IRF was measured over a six-month period with ten x-ray calibration shots of varying x-ray intensities. The IRF was found to be extremely stable over this period with no deviations observed. An average IRF was constructed by normalizing and aligning the measured signals to their peak and is shown in Fig. 154.69 along with the ten measured signals.

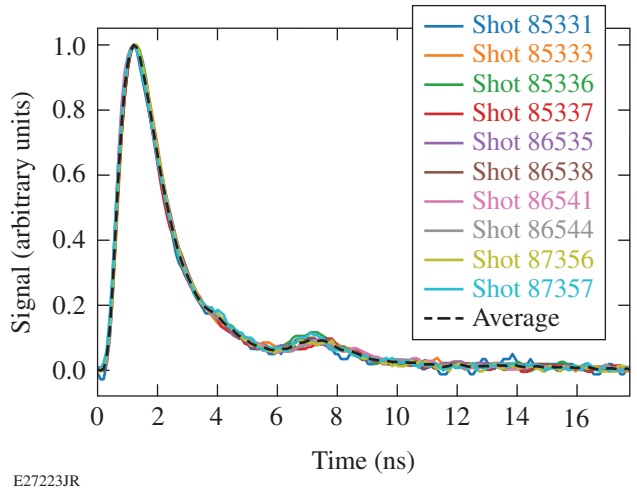

Figure 154.69
The measured x-ray signals from a series of calibration experiments along with the averaged shape. All signal peaks have been aligned in time and normalized. The FWHM of this detector instrument response function is 1.7 ns with a rise time of 0.6 ns. The bump ~5 ns after the main peak is attributed to an ion after pulse unique to the PMT140 used in the detector.

The exponentially modified Gaussian shape of the IRF is characteristic of scintillator detectors, which have a finite excitation lifetime. The average detector IRF has a measured FWHM of 1.7 ns with a rise time of 0.6 ns. The after pulse ~5 ns after the main peak is a unique feature of this detector and is attributed to an ion after pulse,[21] when the applied bias voltage is above 4.6 kV. Decreasing the bias voltage to below 4.6 kV would eliminate the ion after pulse observed but would decrease the PMT gain and the signal-to-noise ratio.

2. Absolute Timing Calibration

To measure the absolute time of flight (TOF) of a signal, the recorded time axis must be calibrated and aligned such that the origin is the moment the signal is produced at TCC. Additionally a calibration is required to eliminate any inherent delay and mistiming in the detector with respect to the OMEGA Hardware Timing System.

To properly time the recorded neutron or x-ray signal to the experiment, measurements of the laser pulse and neutron/x-ray bang times are required. Timing of the laser pulse at TCC is achieved with the p510 streak camera, which measures the laser pulse as it enters the target chamber.[22] The neutron/x-ray bang times are recorded with the NTD.[20] Each of these times is measured relative to the OMEGA timing fiducial. By injecting the same timing fiducial into the recorded neutron or x-ray signal, these measured quantities can be used to properly align the recorded signal with the experiment.

The transformation from a recorded signal time τ, which has an arbitrary timing origin, to the true TOF of the signal t, which is timed to the experiment, is given by

$$t = \tau - \left(\tau_0 + \Delta t_{\text{laser}} + \Delta t_{\text{bang}}\right) - \Delta t_{\text{cal}} - \Delta t_{\text{att}}, \qquad (3)$$

where τ_0 is the time of the measured fiducial on the recorded signal; Δt_{laser} is the delay between the start of the laser pulse (defined as 2% of the maximum laser power) and the fiducial as reported by the p510 streak camera; Δt_{bang} is the delay between the neutron/x-ray bang time and the beginning of the laser pulse as reported by the NTD; Δt_{cal} is a calibration constant accounting for any inherent delays and mistiming in our detector device; and Δt_{att} accounts for additional delays in the signal timing if a signal attenuator is used.

To determine Δt_{cal}, a particle i with a known TOF t_i is recorded and the measured TOF τ_i is determined. Asserting that the known TOF is t_i, Eq. (3) can be solved for Δt_{cal} by using the measured laser pulse and bang time. X-ray signals are ideal for timing-calibration experiments because the TOF is uniquely determined by the detector distance. The x-ray signals used to construct the IRF are used for this timing calibration.

The most accurate method to measure τ_x, the uncalibrated x-ray TOF, is a template-fitting algorithm.[23,24] This method relies on fitting a scaled and translated version of a template signal to the measured data. The main advantage of this technique is that there is no ambiguity in the starting time of the signal and all timing delays are included in the template function used for the fit.

In our application the template signal $m(t)$ is the averaged IRF shown in Fig. 154.69. The actual fitting function is given by

$$g\left(\tau; A, \tau_x\right) = A\, m\left(\tau - \tau_x\right). \qquad (4)$$

In practice, $m(t)$ is a cubic spline interpolation of the template function. Once this function is constructed, a least squares fit can be performed on a measured x-ray pulse to determine A and τ_x. An example of this fit is shown for shot 87356 in Fig. 154.70.

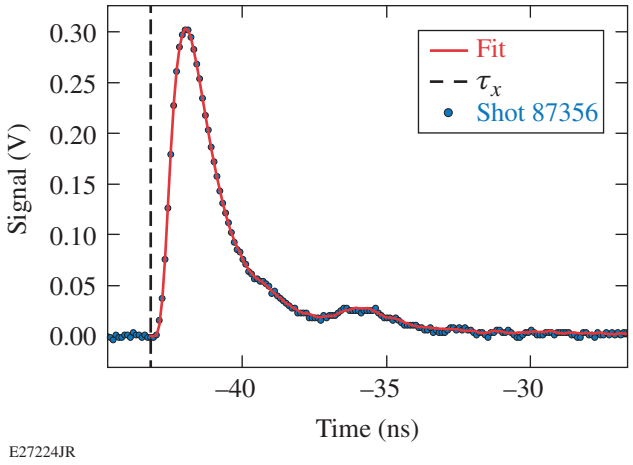

Figure 154.70
Template fit for x-ray shot 87356 to determine τ_x. The best-fit values are A = 0.303±0.001 V and τ_x = –43.162±0.002 ns. Note that the fit is preformed in the uncalibrated time axis of the oscilloscope, so the absolute value of the time holds no significance.

The template-fitting algorithm has been applied to determine τ_x and therefore Δt_{cal} for the eight x-ray calibration shots in **Instrument Response Function** (p. 120), which had a timing fiducial. Figure 154.71 shows the inferred calibration constant for each shot. The average calibration constant from these shots was determined to be Δt_{cal} = 18.840±0.067 ns.

The uncertainty in each measurement of Δt_{cal} was determined by considering the statistical and systematic uncertainties in the measurement. The systematic timing uncertainty

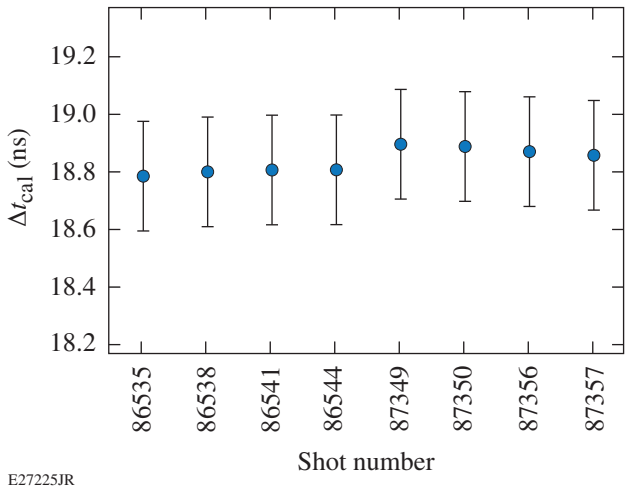

Figure 154.71
The measured calibration constant for the eight x-ray calibration shots with a timing fiducial, each with an uncertainty of ~190 ps. The average calibration constant was measured to be Δt_{cal} = 18.840±0.067 ns.

in t_x is determined by the detector volume. Assuming photon interactions are equally probable throughout the scintillator volume results in a time spread of ~183 ps. There is a statistical uncertainty associated with any fit in the recorded signal time τ, including τ_x, of ~2 ps as well as in the fiducial signal time τ_0 of ~1 ps. The total uncertainty for the terms Δt_{laser} and Δt_{bang} are ~5 ps and ~50 ps, respectively. The uncertainty in the term Δt_{att} has been measured to be ~1 ps. Adding each term in quadrature results in a total timing uncertainty of ~190 ps. The total uncertainty in the average Δt_{cal} has been reduced to ~67 ps by averaging all eight measurements.

The uncertainties in the nTOF are identical as above but include the systematic uncertainty in Δt_{cal} of ~67 ps. Adding the uncertainty of each term in Eq. (3) in quadrature, the total nTOF uncertainty is ~84 ps. This timing uncertainty corresponds to a total neutron energy uncertainty of ~10 keV and a bulk collective velocity uncertainty of ~17 km/s.

If the inferred ion temperature from the neutron energy spectrum is inflated because of nonthermal components to the second central moment associated with fluid motion,[7,11] the thermal component to the first moment[6] will also be inflated. Since the inferred ion temperature is always greater than or equal to the thermal temperature,[11] and the thermal component to the first moment is a monotonically increasing function of ion temperature,[6] a larger thermal component to the first moment is always predicted. To compensate for this, a bulk collective motion away from the detector will be inferred. This effect has been estimated with Monte Carlo calculations, and it was found that a 0.75-keV overprediction of the thermal temperature would lead to a systematic error of, at most, –6 km/s.

Measurements

The nTOF signal for a series of nominal cryogenic and room-temperature experiments has been measured, and the time axes have been calibrated using Eq. (3). To determine the moments of the neutron energy spectrum, the forward-fit method[19] was applied using the averaged IRF measured in **Instrument Response Function** (p. 120). Shifts in the mean neutron energy were then interpreted as bulk collective fluid motion with the use of Eqs. (1) and (2).

Example nTOF traces for two consecutive cryogenic targets are shown in Fig. 154.72. The large difference in the first moment of these signals corresponds to a difference in the mean neutron energy of ~68 keV and a difference in fluid velocity of ~125 km/s. The measured neutron yield and minimum measured DT ion temperature were 1.01×10^{14} and 3.9 keV for shot

86181 and 1.06×10^{14} and 4.5 keV for shot 86184, respectively. The target offset for shot 86181 was –32 μm along the OMEGA P7 direction, which can explain the observed large flow away from the detector.

Figure 154.73 shows inferred hot-spot fluid velocity for each experiment. Large variations in the inferred flow velocities are observed in cryogenic experiments but not in room-temperature implosions, indicating residual motion of the hot spot at peak neutron production may exist for cryogenic implosions. Additionally, cryogenic experiments show a systematic flow toward the detector, suggesting a systematic flow of 42 km/s along the OMEGA P7 axis while the average flow for room-temperature experiments is –6 km/s.

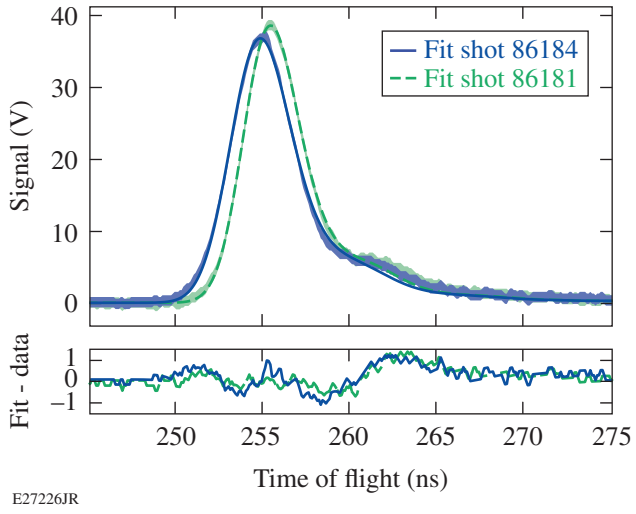

Figure 154.72
The measured nTOF signal bounded by signal noise ±1σ (blue-shaded area) with the corresponding forward fit (solid blue curve) for two consecutive cryogenic shots 86181 and 86184. The TOF shift corresponds to a difference in fluid velocity of ~125 km/s, indicating residual motion of the hot spot in each shot.

Conclusion

A new nTOF detector capable of measuring the absolute neutron energy spectrum has been fielded on the OMEGA laser. The detector IRF has been measured *in situ* and has been calibrated with x-ray timing experiments. A method has been described to infer bulk fluid velocity of the neutron-producing region in ICF experiments; measurements of this motion in cryogenic targets show velocities as large as 103±17 km/s.

Future work will extend this analysis to multiple lines of sight to determine the complete bulk fluid velocity vector. Extending this measurements to three LOS would allow for the determination of the three components of the bulk fluid velocity vector. With four measurements of the neutron mean energy, each component of the bulk collective velocity could be determined in addition to the thermal temperature, without relying on measurements of the second moment. This would eliminate the systematic uncertainty associated with the nonthermal component of the second moment discussed in **Absolute Timing Calibration** (p. 121), which leads to a decrease in the inferred flows.

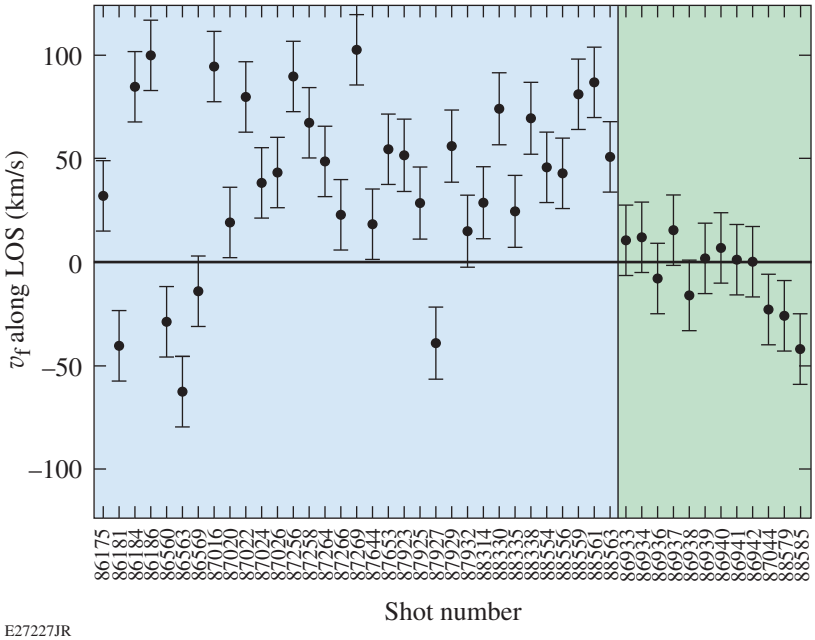

Figure 154.73
The inferred bulk collective velocity for a series of cryogenic implosions (blue-shaded area) and room-temperature implosions (green-shaded area). There are significant variations in the inferred flows in cryogenic targets, indicating residual motion of the hot spot. Additionally a systematic flow toward the P7 port is observed for cryogenic experiments.

ACKNOWLEDGEMENT

This material is based upon work supported by the Department of Energy National Nuclear Security Administration under Award Number DE-NA0001944, the University of Rochester, and the New York State Energy Research and Development Authority.

REFERENCES

1. R. C. Shah, B. M. Haines, F. J. Wysocki, J. F. Benage, J. A. Fooks, V. Glebov, P. Hakel, M. Hoppe, I. V. Igumenshchev, G. Kagan, R. C. Mancini, F. J. Marshall, D. T. Michel, T. J. Murphy, M. E. Schoff, K. Silverstein, C. Stoeckl, and B. Yaakobi, Phys. Rev. Lett. **118**, 135001 (2017).

2. P. B. Radha, T. J. B. Collins, J. A. Delettrez, Y. Elbaz, R. Epstein, V. Yu. Glebov, V. N. Goncharov, R. L. Keck, J. P. Knauer, J. A. Marozas, F. J. Marshall, R. L. McCrory, P. W. McKenty, D. D. Meyerhofer, S. P. Regan, T. C. Sangster, W. Seka, D. Shvarts, S. Skupsky, Y. Srebro, and C. Stoeckl, Phys. Plasmas **12**, 056307 (2005).

3. B. K. Spears, M. J. Edwards, S. Hatchett, J. Kilkenny, J. Knauer, A. Kritcher, J. Lindl, D. Munro, P. Patel, H. F. Robey, and R. P. J. Town, Phys. Plasmas **21**, 042702 (2014).

4. I. V. Igumenshchev, D. T. Michel, R. C. Shah, E. M. Campbell, R. Epstein, C. J. Forrest, V. Yu. Glebov, V. N. Goncharov, J. P. Knauer, F. J. Marshall, R. L. McCrory, S. P. Regan, T. C. Sangster, C. Stoeckl, A. J. Schmitt, and S. Obenschain, Phys. Plasmas **24**, 056307 (2017).

5. H. Brysk, Plasma Phys. **15**, 611 (1973).

6. L. Ballabio, J. Källne, and G. Gorini, Nucl. Fusion **38**, 1723 (1998).

7. B. Appelbe and J. Chittenden, Plasma Phys. Control. Fusion **53**, 045002 (2011).

8. B. Appelbe and J. Chittenden, High Energy Density Phys. **11**, 30 (2014).

9. D. H. Munro, Nucl. Fusion **56**, 036001 (2016).

10. D. H. Munro *et al*., Phys. Plasmas **24**, 056301 (2017).

11. T. J. Murphy, Phys. Plasmas **21**, 072701 (2014).

12. A. B. Zylstra, M. Gatu Johnson, J. A. Frenje, F. H. Séguin, H. G. Rinderknecht, M. J. Rosenberg, H. W. Sio, C. K. Li, R. D. Petrasso, M. McCluskey, D. Mastrosimone, V. Yu. Glebov, C. Forrest, C. Stoeckl, and T. C. Sangster, Rev. Sci. Instrum. **85**, 063502 (2014).

13. M. Gatu Johnson, D. T. Casey, J. A. Frenje, C.-K. Li, F. H. Séguin, R. D. Petrasso, R. Ashabranner, R. Bionta, S. LePape, M. McKernan, A. Mackinnon, J. D. Kilkenny, J. Knauer, and T. C. Sangster, Phys. Plasmas **20**, 042707 (2013).

14. R. A. Lerche *et al*., Appl. Phys. Lett. **31**, 645 (1977).

15. V. Yu. Glebov, presented at the nTOF Diagnostic Workshop at Lawrence Livermore National Laboratory, Livermore, CA, 18 July 2017.

16. V. Gopalaswamy, R. Betti,J. P. Knauer, A. Bose, N. Luciani, I. V. Igumenshchev, K. S. Anderson, K. A. Bauer, M. J. Bonino, E. M. Campbell, D. Cao, A. R. Christopherson, G. W. Collins, T. J. B. Collins, J. R. Davies, J. A. Delettrez, D. H. Edgell, R. Epstein, C. J. Forrest, D. H. Froula, V. Yu. Glebov, V. N. Goncharov, D. R. Harding, S. X. Hu, D. W. Jacobs-Perkins, R. T. Janezic, J. H. Kelly, O. M. Mannion, F. J. Marshall, D. T. Michel, S. Miller, S. F. B. Morse, D. Patel, P. B. Radha, S. P. Regan, S. Sampat, T. C. Sangster, A. B. Sefkow, W. Seka, R. C. Shah, W. T. Shmyada, A. Shvydky, C. Stoeckl, W. Theobald, K. M. Woo, J. D. Zuegel, M. Gatu Johnson, R. D. Petrasso, C. K. Li, and J. A. Frenje "Tripling the Fusion Yield in Direct-Drive Laser Fusion Through Predictive Statistical Modeling," to be submitted to Nature.

17. Eljen Technology, Sweetwater, TX 79556.

18. Photek Ltd., St. Leonards on Sea, East Sussex, TN38 9NS, United Kingdom.

19. R. Hatarik, D. B. Sayre, J. A. Caggiano, T. Phillips, M. J. Eckart, E. J. Bond, C. Cerjan, G. P. Grim, E. P. Hartouni, J. P. Knauer, J. M. Mcnaney, and D. H. Munro, J. Appl. Phys. **118**, 184502 (2015).

20. C. Stoeckl, R. Boni, F. Ehrne, C. J. Forrest, V. Yu. Glebov, J. Katz, D. J. Lonobile, J. Magoon, S. P. Regan, M. J. Shoup III, A. Sorce, C. Sorce, T. C. Sangster, and D. Weiner, Rev. Sci. Instrum. **87**, 053501 (2016).

21. N. Kishimoto *et al*., Nucl. Instrum. Methods Phys. Res. A **564**, 204 (2006).

22. W. R. Donaldson, R. Boni, R. L. Keck, and P. A. Jaanimagi, Rev. Sci. Instrum. **73**, 2606 (2002)

23. B. W. Adams *et al*., Nucl. Instrum. Methods Phys. Res. A **795**, 1 (2015).

24. W. E. Cleland and E. G. Stern, Nucl. Instrum. Methods Phys. Res. A **338**, 467 (1994).